Deep elastic strain engineering of bandgap through machine learning

Zhe Shi[a,b,1], Evgenii Tsymbalov[c,1], Ming Dao[a], Subra Suresh[d,2], Alexander Shapeev[c,2], and Ju Li[a,b,2]

[a]Department of Materials Science and Engineering, Massachusetts Institute of Technology, Cambridge, MA 02139; [b]Department of Nuclear Science Engineering, Massachusetts Institute of Technology, Cambridge, MA 02139; [c]Skolkovo Institute of Science and Technology, 121205 Moscow, Russia; and [d]Nanyang Technological University, 639798 Singapore, Republic of Singapore

Nanoscale specimens of semiconductor materials as diverse as silicon and diamond are now known to be deformable to large elastic strains without inelastic relaxation. These discoveries harbinger a new age of deep elastic strain engineering of the band structure and device performance of electronic materials. Many possibilities remain to be investigated as to what pure silicon can do as the most versatile electronic material and what an ultrawide bandgap material such as diamond, with many appealing functional figures of merit, can offer after overcoming its present commercial immaturity. Deep elastic strain engineering explores full six-dimensional space of admissible nonlinear elastic strain and its effects on physical properties. Here we present a general method that combines machine learning and ab initio calculations to guide strain engineering whereby material properties and performance could be designed. This method invokes recent advances in the field of artificial intelligence by utilizing a limited amount of ab initio data for the training of a surrogate model, predicting electronic bandgap within an accuracy of 8 meV. Our model is capable of discovering the indirect-to-direct bandgap transition and semiconductor-to-metal transition in silicon by scanning the entire strain space. It is also able to identify the most energy-efficient strain pathways that would transform diamond from an ultrawide-bandgap material to a smaller-bandgap semiconductor. A broad framework is presented to tailor any target figure of merit by recourse to deep elastic strain engineering and machine learning for a variety of applications in microelectronics, optoelectronics, photonics, and energy technologies.

electronic band structure | bandgap engineering | first-principles calculation | neural network | semiconductor materials

Nanostructured materials can withstand extremely large deformation without mechanical relaxation or failure compared with their conventional counterparts, opening up a vast parameter space for rational engineering of material properties by tensorial elastic strain. The electronic, optical, thermal, and chemical properties of crystals are functions of the six-dimensional elastic strain tensor ε ($\varepsilon_1 \equiv \varepsilon_{11}$, $\varepsilon_2 \equiv \varepsilon_{22}$, $\varepsilon_3 \equiv \varepsilon_{33}$, $\varepsilon_4 \equiv \varepsilon_{23}$, $\varepsilon_5 \equiv \varepsilon_{13}$, $\varepsilon_6 \equiv \varepsilon_{12}$ following the so-called Voigt notation), which provides a continuously tunable set of variables analogous to the chemical composition of a seven-element alloy. Electronic bandgap E_g opens or closes with ε, resulting in drastic alteration of the electrical, thermal, optical, and magnetic characteristics (1). With the proliferation of ultrastrength nanostructured materials that can sustain a wide range of nonhydrostatic and potentially dynamically varying stresses (2), and various miniaturization-enabled means of applying ε (3), a historical window of opportunity has now opened up to scan a vast unexplored space for the development of materials and devices with desirable combinations of physical and functional properties (4). For example, while it is well known that unstrained Si has an electronic bandgap of 1.1 eV, we know that, when subjected to an equibiaxial strain of 5%, it would have a different bandgap. Furthermore, a 5% tensile strain on Si would produce a different bandgap from a 5% shear strain. At large strains, all these differently strained pure Si crystals would not behave as the unstrained "typical silicon." An added benefit is that

with strain engineering, it is in principle possible to dynamically change the mechanical actuation, and switch between these differently strained materials, something that bandgap engineering by chemical means such as molecular beam epitaxy cannot accomplish. Not only the value of E_g, but also its character (e.g., direct or indirect), and the topological features of a band structure can be changed with ε before the ideal strain surface [a five-dimensional (5D) surface] $f(\varepsilon_1, \varepsilon_2, \varepsilon_3, \varepsilon_4, \varepsilon_5, \varepsilon_6) = 0$ in six dimensions (6D) is reached (5).

Over the past two decades, elastic strain engineering (ESE) has achieved one substantial commercial success (6): strained silicon technology, where a biaxial elastic strain of the order of 1% applied to a thin channel of silicon enhances the mobility of charge carriers by more than 50% and increases central processing unit (CPU) clock speed correspondingly. Recent studies have shown that nanowires of silicon can sustain a tensile elastic strain of as much as 16% (7), while nanoscale needles of diamond can be bent to a local maximum tensile elastic strain in excess of 9% (8). As we show in this paper, if we are able to exploit the ability of Si and C to deform up to strains of these magnitudes under certain conditions, there exist much greater possibilities than what is currently realized for engineering of band structure and bandgap for a wide variety of electronic, optoelectronic, and photonic materials employed in communication,

Significance

Deforming a material to a large extent without inelastic relaxation can result in unprecedented properties. However, the optimal deformation state is buried within the vast continua of choices available in the strain space. Here we advance a unique and powerful strategy to circumvent conventional trial-and-error methods, and adopt artificial intelligence techniques for rationally designing the most energy-efficient pathway to achieve a desirable material property such as the electronic bandgap. The broad framework for tailoring any target figure of merit, for any material using machine learning, opens up opportunities to adapt elastic strain engineering of properties and performance in devices and systems in a controllable and efficient manner, for potential applications in microelectronics, optoelectronics, photonics, and energy technologies.

information, and energy applications that impact every aspect of modern life (9).

ESE seeks to identify metastable states of matter for optimizing functional properties and performance. A strained material is in a state of higher energy than when it is in a stress-free state, characterized by the strain-energy density h which is measured in units of meV/Å³. Therefore, addressing the following question is at the heart of ESE: What is the energy cost (h) to achieve the desired property change? Consider the challenges of reducing the bandgap of Si from 1.1 eV in its stress-free state to 0 eV in a metal-like state, or converting diamond from an ultrawide-bandgap material into a wide or even medium-bandgap material so that the full potential of its many appealing characteristics for microelectronics and optoelectronics could be realized. To achieve the above transitions in the most efficient manner, it is important to design ε through the most optimal combination of its normal and shear components.

To address the foregoing question, we resort to deep ESE which exploits the latest advances in artificial intelligence and multiscale modeling. To set the scene, consider a situation where it is desirable to examine all possible combinations of the components of ε, over a range of potential interest, say between −10 and +10% in each strain component. Here, say that the objective is to determine the least energetically expensive route to alter the bandgap of a material by a desired amount. Although ab initio calculations such as those involving many-body corrections can provide accurate energy-band results, the scope of such calculations is somewhat limited to about 1,000 strain points because of high computational cost. On the other hand, by discretizing ε with a regular grid comprising 20 nodes separated at each 1% strain interval over the strain range of −10 to +10%, the computational model would entail about 10^8 band structures, up to five orders of magnitude higher computational requirement than what can be reasonably achieved presently. To overcome these difficulties, we present here a general method that combines machine learning (ML) and ab initio calculations to identify pathways to ESE. This method invokes artificial neural networks (NNs) to predict, to a reasonable degree of accuracy, material properties as functions of the various input strain combinations on the basis of only a limited amount of data. We also demonstrate the potential of our method for bandgap engineering with specific calculations for perfect crystals of Si and diamond. These two materials bookend the wide spectrum of current possibilities and potential opportunities for optimizing the performance of semiconductor materials and devices. Si, on the one hand, represents the most widely used and commercially successful semiconductor material. Diamond, on the other hand, represents the most appealing ultrawide-bandgap material due to its extremely high thermal conductivity and hardness, high electron/hole mobilities and saturation drift velocities, and breakdown field (10). Tuning bandgap, and more broadly the band structure, through deep ESE provides opportunities for tapping into the many appealing figures of merit for device performance of any material. Moreover, we choose Si, the most versatile electronic material, to demonstrate that our ML machinery is capable of predicting important physical phenomena such as indirect-to-direct bandgap transition and semiconductor-to-semimetal transition. We also visualize silicon's "paleolith"-like isobandgap surfaces in strain space, akin to the yield surface commonly used to describe the plastic deformation of metallic materials, but with sharp ridges and corners that reflect band-edge cross-overs.

Results

ML and Density of States of Bandgap. We aim to describe the electronic bandgap and band structure as functions of strain by training ML models on first-principles density-functional theory (DFT) data. This approach leads to reasonably accurate training with much fewer computed data than fine-grid ab initio calculations and a fast evaluation time. The DFT calculations were conducted in two settings: a large, computationally inexpensive Perdew–Burke–Ernzerhof (10) (PBE) dataset obtained for fitting

and a small but accurate many-body GW [G, Green's function; W, screened Coulomb interaction (11)] dataset for correction. As depicted in Fig. 1A, the strain tensor and/or the **k**-point coordinates are fed into different ML models as input to fit or make predictions about energy eigenvalues or bandgap. Table 1 demonstrates the accuracy of these models on the PBE data, the best of which is attained by the NN. The data fusion technique (12, 13) is adopted to further improve the learning outcome of bandgap. The resulting model allows the prediction of bandgap to reach an extremely high accuracy of 8 meV in the mean absolute error (MAE), as shown in Fig. 1B and *SI Appendix*, Table S1. The successful combination of the quantitative advantage of PBE and the qualitative advantage of GW results in a bandgap-prediction model with a level of accuracy comparable to experiments.
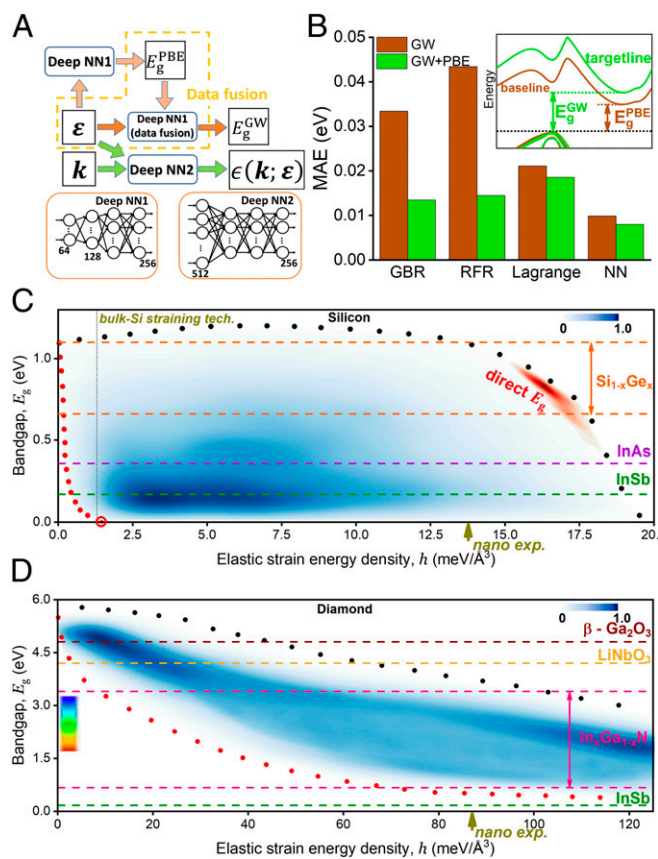
Fig. 1. (*A*) ML workflow with NN. For a typical bandgap-prediction task, the input contains the strain information only and the target is either E_g^{PBE} or E_g^{GW}. In the data fusion process, the bandgap predicted from fitting the PBE dataset is also taken in as an input to fit the GW bandgap. For the whole band structure fitting task, the input contains both strain information and the **k**-point coordinates and the target is the energy dispersion $\varepsilon_n(\mathbf{k}; \varepsilon)$, where n is the band index, **k** is the wavevector, and ε is the crystal strain tensor. The hidden-layer structures of the two associated deep NNs are also depicted. (*B*) Better bandgap-fitting results measured by MAE are yielded by data fusion compared with the sole use of ε as input to fit GW data. (*Inset*) Data-fusion-based learning of the difference between E_g^{PBE} and E_g^{GW}. Ensemble methods on decision-tree classifiers including gradient boosting regression (GBR) and random forest regression (RFR), Lagrange interpolation and NN are adopted for ML fitting. (*C*) Reachable bandgap values for various h within the whole deformation space for silicon. The region where the strained silicon has a direct bandgap is colored in red. The circle at $h = 1.35$ meV/Å³ indicates the lowest energy penalty for the semiconductor-to-metal transition. (*D*) Diamond bandgap envelope extending toward the small-bandgap semiconductor region. The upper- and lower-envelope functions are indicated by black and red dots, respectively. The arrows on the horizontal axes in *C* and *D* indicate reachable h by the in situ experiments (7, 8).

Table 1. Root-mean-squared error for various ML algorithms for the bandgap and band structure prediction tasks from PBE data for silicon (in units of electron volts)

ML input	ML algorithms			ML target
	GBR	RFR	NN	
ε^{3D}	0.0367	0.0247	0.0049	Bandgap
ε^{6D}	0.0743	0.0781	0.0264	Bandgap
k and ε^{6D} VB	0.1125	0.1078	0.0131	$\epsilon_n(\mathbf{k};\varepsilon)$
k and ε^{6D} CB	0.1593	0.1555	0.0184	$\epsilon_n(\mathbf{k};\varepsilon)$

ε^{3D} and ε^{6D} denote three-normal-strains deformation and general deformation cases, respectively. For all of the details on ML and DFT methodology, optimization, and implementation, see *Methods* and *SI Appendix*, Notes S1 and S2 and Figs. S1 and S2.

In ESE experiments, the objective is to identify the highest or lowest bandgap that can be achieved through the expenditure of a certain elastic strain energy density (h) defined as

$$h(\varepsilon) \equiv \frac{E(\varepsilon) - E^0}{V^0}, \qquad [1]$$

where $E(\varepsilon)$ is the total energy of the cell deformed by strain ε, and E^0 and V^0 are the total energy and volume of the undeformed cell, respectively. Here, we data-mine the 6D deformation by ML the bandgap distribution and the elastic strain energy density against ε. The many-to-many relation between $h(\varepsilon)$ and the bandgap $E_g(\varepsilon)$ is shown in Fig. 1 *C* and *D*. In the stress-free equilibrium state, silicon has a bandgap of 1.1 eV; with an increase in strain energy density, a variety of possible bandgaps emerge. Even silicon with as little strain energy density as 0.2 meV/Å^3 can become quite a different material from the stress-free silicon. As h further increases, the largest allowable bandgap drops and an "envelope" forms, as evidenced by the change of maximal and minimal bandgap reachable under a fixed h. The shading of the envelope regions in Fig. 1 *C* and *D* reflects the distribution of the available bandgap. A darker shading qualitatively indicates that the amount of possible strains to achieve a specific bandgap at a given h is higher. Outside the envelope the shading color is white, meaning that the corresponding bandgap is not attainable. Mathematically, we can define the cumulative "density of states" of bandgap as

$$c(E_g'; h') \equiv \int\limits_{h(\varepsilon) < h'} d^6\varepsilon\, \delta\big(E_g' - E_g(\varepsilon)\big)$$

$$= \int d^6\varepsilon\, \delta\big(E_g' - E_g(\varepsilon)\big) H\big(h' - h(\varepsilon)\big), \qquad [2]$$

where $d^6\varepsilon \equiv d\varepsilon_1 d\varepsilon_2 d\varepsilon_3 d\varepsilon_4 d\varepsilon_5 d\varepsilon_6$ in the 6D strain space, $\delta(\cdot)$ is the Dirac delta function, and $H(\cdot)$ is the Heaviside step function. We then define the density of states of bandgap (DOB) at h' by taking the derivative of $c(E_g'; h')$ with respect to h':

$$\rho(E_g'; h') \equiv \frac{\partial c(E_g'; h')}{\partial h'} = \int d^6\varepsilon\, \delta\big(E_g' - E_g(\varepsilon)\big) \delta(h' - h(\varepsilon)). \qquad [3]$$

The meaning of DOB can be described by considering all possible elastically strained states within the $\left(h - \frac{dh}{2}, h + \frac{dh}{2}\right)$ energy interval, and the resultant distribution of bandgaps arising from these states. The DOB function $\rho(E_g; h)$ offers a blueprint for determining which bandgaps are accessible at what energy cost. One can use the definition (3) not only for the electronic bandgap, but also generally for any scalar property that will provide

an easy-to-visualize map for deep ESE such as the thermoelectric figure of merit zT, Baliga's figure of merit (14), Curie temperature, etc. (4). An upper-envelope function $E_g^{\text{upper}}(h)$ and lower-envelope function $E_g^{\text{lower}}(h)$ can also be defined based on $\rho(E_g; h)$:

$$E_g^{\text{upper}}(h) \equiv \max \text{supp}_{E_g}\big(\rho(E_g; h)\big),$$
$$E_g^{\text{lower}}(h) \equiv \min \text{supp}_{E_g}\big(\rho(E_g; h)\big), \qquad [4]$$

which are rendered as black and red dotted lines in Fig. 1 *C* and *D*, so the nonzero DOB falls within $(E_g^{\text{lower}}(h), E_g^{\text{upper}}(h))$. In deep ESE, $E_g^{\text{lower}}(h)$ also indicates the path to obtain the fastest change in E_g. For instance, if the goal is to reduce the bandgap of silicon from 1.1 eV as fast as possible, with the least cost of elastic energy, the red-dotted line in Fig. 1*C* (which is further detailed in Fig. 2*A*) $E_g^{\text{lower}}(h)$ offers the best design of the strain tensor ε to achieve this goal.

It is seen from Fig. 1 *C* and *D* that, with the application of a relatively small amount of mechanical energy, the overall distribution of Si bandgap shifts downward. This means that by modulating the tensorial strain (shear/tension/compression combinations) in multiple directions, strained silicon becomes capable of absorbing a different part of the electromagnetic spectrum than when it is in a stress-free state. It was also found that at 1.35 meV/Å^3 the bandgap of Si can vanish, corresponding to the minimum energy required for semiconductor-to-metal transition in the whole 6D strain space (see Fig. 2*B* for the band structure, which corresponds to the red circle in Fig. 1*C*). Fig. 2*A* further illustrates that silicon's "most energy efficient path to metallization" is actually a curved path in the strain space: The initial fastest-descent direction for E_g (at $h = 0$) is quite different from when E_g hits zero at $h = 1.35$ meV/Å^3 and thus linear perturbation theory such as the deformation potential theory (15) is not expected to work well in deep-strain space. It is not straightforward yet to achieve this complex optimal strain state in 6D experimentally, despite Feynman's prophecy to use "a hundred tiny hands" (3). To provide experimental guidance, we further implemented our ML model in experimentally feasible uniaxial strain cases. It is found that $\langle 111 \rangle$ crystal direction is the most energy-efficient uniaxial strain direction for Si bandgap engineering (*SI Appendix*, Fig. S3). A complete ranking of the common crystal directions in terms of their ability to lower Si bandgap can be found in *SI Appendix*, Note S3. In the case of diamond, deep ESE provides an opportunity to reduce its bandgap to a level comparable to that of InAs. Our results thus demonstrate that by straining diamond in the most optimal way, it can be transformed to mimic the properties of a lower-bandgap semiconductor while almost preserving its own uniqueness such as high strength and thermal conductivity, thereby
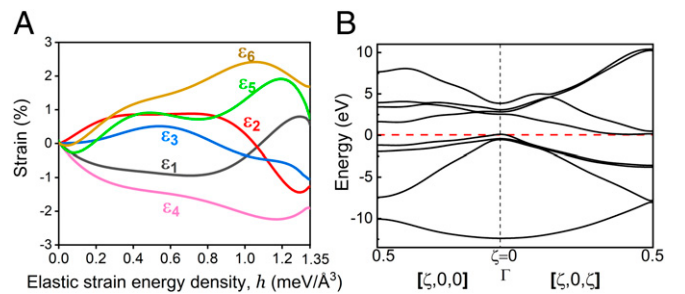
Fig. 2. (*A*) The most energy-efficient strain pathway to reach the zero-bandgap state, i.e., the lower-envelope function $E_g^{\text{lower}}(h)$ in silicon corresponding to the red-dotted line in Fig. 1*C*. The zero-bandgap state (open red circle on the horizontal axis of Fig. 1*C*) corresponds to the deformation case of $\varepsilon_1 = 0.5522\%$, $\varepsilon_2 = -1.2582\%$, $\varepsilon_3 = -1.036\%$, $\varepsilon_4 = -1.9168\%$, $\varepsilon_5 = 0.7411\%$, and $\varepsilon_6 = 1.6878\%$. (*B*) GW band structure associated with this deformation. The fractional coordinates for the three high-symmetry points along the selected **k** path are (0.5, 0, 0), (0, 0, 0), and (0.5, 0, 0.5), respectively.

paving the way for designing hitherto unexplored combinations of material characteristics.

Another important issue for optical applications pertains to whether the bandgap is direct or indirect. This direct bandgap envelope is a subset of DOB. We define the density of direct bandgaps (DOD) in parallel to [2]–[4], but with $E_{\text{direct g}}$ instead of E_g, to obtain DOD $\rho_d(E_{\text{direct g}}; h)$ and its bounds $E_{\text{direct g}}^{\text{upper}}(h)$, $E_{\text{direct g}}^{\text{lower}}(h)$. Obviously, if direct bandgaps exist at any strain, for that strain there will be

$$\left(E_{\text{direct g}}^{\text{lower}}(h), E_{\text{direct g}}^{\text{upper}}(h)\right) \subseteq \left(E_g^{\text{lower}}(h), E_g^{\text{upper}}(h)\right). \quad [5]$$

Our deep ESE model found within experimentally accessible strain range that the indirect-to-direct bandgap transition takes place in silicon in the high-h region and a minimum strain energy density $h_d^{\min}$ around 15.4 meV/Å^3 exists for the direct bandgap to appear (the red region in Fig. 1C):

$$h_d^{\min} = \min \text{supp}_h \left(E_{\text{direct g}}^{\text{upper}}(h) - E_{\text{direct g}}^{\text{lower}}(h)\right). \quad [6]$$

This little "island" of DOD within the ocean of DOB can be achieved by applying $\varepsilon_1 = \varepsilon_2 = \varepsilon_3 \geq 9.3\%$.

The conventional way to modulate electronic properties in semiconductors is the so-called compositional grading technique. Through varying the stoichiometry of an alloy semiconductor, as for example by molecular beam epitaxy, a graded bandgap can be produced (16). This method of tweaking the material property is conceptually based on chemical alloying, whereby the chemical composition is tuned in an alloy melt to produce desirable strength or ductility. Invoking this approach, conventional bandgap engineering resorted to chemical alloying such as GaAl$_{1-x}$As$_x$ or Ga$_{1-x}$In$_x$As (17). However, we have demonstrated here that the stress-free situation is usually not the optimal state for a figure of merit, and elastic strains allow the bandgap to exhibit many more possible values so that each pure material candidate should occupy a much larger hyperspace enabled through the achievable 6D strain space. The more general bandgap engineering approach could utilize gradients in both composition and strain to achieve the desired band alignment.

Exploring Bandgap Ridgelines in Strain Space. Here we choose the most widely used semiconductor material, Si, as an example to demonstrate the generality and flexibility of our method. Since the full 6D strain space does not allow for easy visualization, we restrict ourselves to tensile and compressive normal strains only ($\varepsilon_4 = \varepsilon_5 = \varepsilon_6 = 0$) for illustration purposes. Note that combinations of tensile and compressive strains can be used to generate shear strains in the material even though not all shear strains are considered. Fig. 3A illustrates the isosurface for Si bandgap, i.e., the set of points in the strain space where the bandgap equals some given value, for different E_g levels obtained by our high-throughput NN model. The most striking visual feature of this E_g isosurface in $\varepsilon_1\varepsilon_2\varepsilon_3$ space is its piecewise smoothness. There are cusp singularities of different order: ridgelines where two smooth pieces of the E_g isosurface meet, and corners where three ridgelines meet. These singularities are characterized by discontinuities in the slope (but not value) of the isosurface in the strain space due to band cross-over or even band topology change. Such cusp features also exist in E_g isosurface in the general-$\varepsilon_1\varepsilon_2\varepsilon_3\varepsilon_4\varepsilon_5\varepsilon_6$ space, although they are more difficult to visualize directly. One can mathematically define these nonsmooth features on the 5D isosurface (embedded in 6D) as nth-order ridges (E_g) if they are differentiable in 5-n directions, while sustaining a change in slope in the other n directions in the strain space.

Since both the crystal structure and deformation tensor have symmetries, and the bandgap as a function of strain is invariant with respect to some of them, the "paleolith"-like E_g isosurface (in analogy to the Tresca yield surface in strength of materials) has the following symmetry structure:
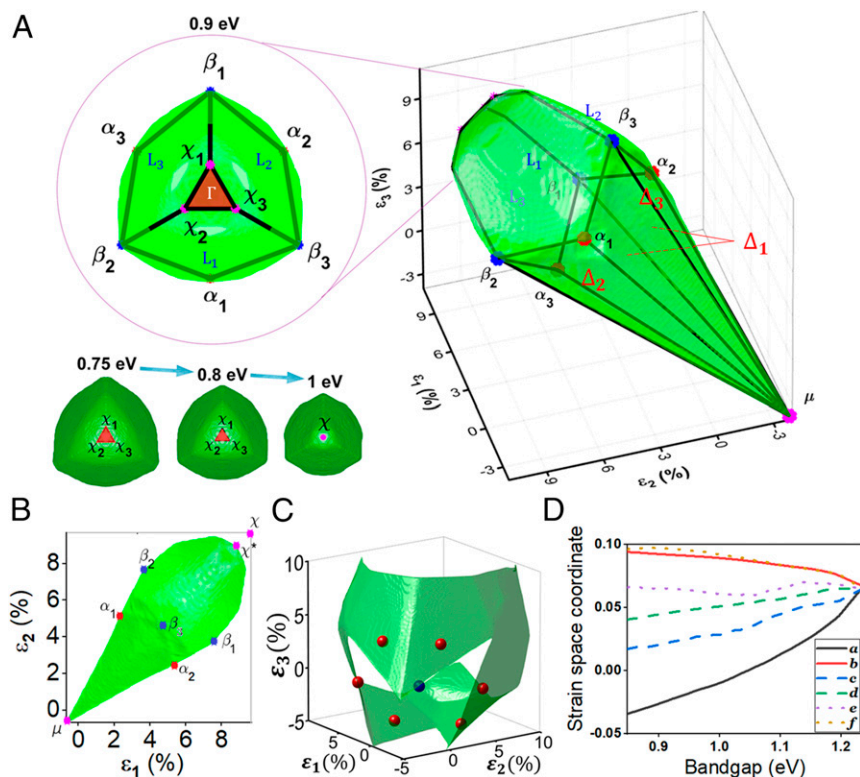
Fig. 3. (A) Bandgap isosurfaces for silicon in the $\varepsilon_1\varepsilon_2\varepsilon_3$ strain space appear to have the paleolith shape for every E_g level. The main corners ($\chi, \mu, \alpha_i, \beta_j$) of an isosurface at $E_g = 0.9$ eV are indicated by different colors and the "carapaces" are distinguished by their associated **k**-space CBM labels. The red triangular faces indicate the direct-bandgap region at different E_g levels. As bandgap increases, the area for the red triangle eventually shrinks to a single χ point. GW model was used. (B) Bandgap isosurface shown through the $\varepsilon_1 - \varepsilon_2$ projection of Si at 1 eV level with GW data. The χ point corresponds to the direct-bandgap case and it splits into three at small E_g as shown in A. (C) Zero-bandgap isosurface in the strain space based on GW data. The blue point corresponds to the strain-free state; red points are strains with the least h of 1.65 meV/Å^3 on this isosurface. (D) Strain-space coordinates of the bandgap isosurface corners (defined as in A) as a function of the bandgap level. The maximum bandgap possible in this strain space is about 1.24 eV, and it is reached at a triaxial strain of 6.5%. In the cases where three χ-type points exist, b equals the average coordinate of them.

i) The points μ (the most "compressive" hydrostatic strain point on the E_g isosurface) and χ (most "tensile" hydrostatic strain point on the E_g isosurface) lie on the $\varepsilon_1 = \varepsilon_2 = \varepsilon_3$ line. We thus denote their strain-space coordinates by (a,a,a) and (b,b,b), respectively. At small or moderate E_g, χ splits and gives rise to a topologically triangular region $\chi_1\chi_2\chi_3$ as shown in Fig. 3*A*. It will later be shown these χ-type points form the direct bandgap region on the E_g isosurface.

ii) The points $\alpha_j (j=1,2,3)$ form a regular triangle which lies in a plane orthogonal to the $\varepsilon_1 = \varepsilon_2 = \varepsilon_3$ line. Their coordinates are denoted by (c,d,d), (d,c,d), and (d,d,c), respectively.

iii) The points $\beta_j (j=1,2,3)$ also form a regular triangle which lies in a plane orthogonal to the $\varepsilon_1 = \varepsilon_2 = \varepsilon_3$ line. Their coordinates are denoted by (f,e,e), (e,f,e), and (e,e,f), respectively.

The shape of the isosurface is similar for both PBE and GW bandgaps, although the specific strain values may differ for the same PBE and GW bandgap levels. It was found that the easiest way [with the least $h(\boldsymbol{\varepsilon}^{3D})$] to obtain the 0-eV bandgap without any shear strain is to apply a normal strain of -3.86 and 4.36% along any two of the three $\langle 100 \rangle$ directions while leaving the third $\langle 100 \rangle$ direction undeformed. Therefore, there are six strain cases that are equivalent, as indicated by red dots in Fig. 3*C*. The position of the vertices of the E_g isosurface in the strain space is the function of selected bandgap value, and the detailed relationship between the bandgap and the strains is shown in Fig. 3*D*. According to our PBE + GW model, the maximum bandgap reachable by strained silicon is 1.24 eV under a hydrostatic tensile strain of 6.5%. It should be noted that silicon strained to such an extent can nearly reach the maximum theoretical efficiency, known as the Shockley–Queisser limit (18), of a single p-n junction solar cell, demonstrating possible application of ESE in solar energy conversion devices.

The formation of the E_g isosurfaces, such as the ones in Fig. 3*A*, is due to the relative position of the valence band maximum (VBM) and the conduction band minimum (CBM). Despite different shape variations of the two energy bands, modulating elastic strain provides possibilities for the VBM and CBM to differ by the same amount with respect to the vacuum level. For undeformed silicon with a bandgap of 1.1 eV, the VBM is located at the Γ point and the CBM lies on the straight line (the Δ line) in the $\mathbf{k}$ space and is positioned at about 85% of the way from the Brillouin zone center to the zone boundary (19). Under 3D deformation, the cubic crystal symmetry of Si is lifted and we follow the $\mathbf{k}$-point labeling scheme explained in *SI Appendix,* Note S1 and Fig. 1 to describe band extrema positions. It is found that VBM remains at Γ irrespective of deformation whereas the position of CBM can be greatly affected by external strains. Using the geometry of the E_g isosurface as a visualization tool, we identify four types of $\mathbf{k}$-space transition in CBM that may happen across the ridgelines on the isosurface.

Starting with the strain points on the lower faces separated by $\mu - \alpha_j$ ridgelines of the E_g isosurface in Fig. 3*A*, we found that the CBM retains roughly the same relative position along the "Δ"-type line as in the undeformed case, and that crossing the ridgelines only switches CBM among $\Delta_1 = (0, k_1, k_1)$, $\Delta_2 = (k_1, 0, k_1)$, and $\Delta_3 = (k_1, k_1, 0)$, where $k_1 \approx 0.425$. In other words, $\mu-\alpha_1$ ridgeline corresponds to Δ_2/Δ_3 transition, $\mu-\alpha_2$ ridgeline corresponds to Δ_1/Δ_3 transition, $\mu-\alpha_3$ ridgeline corresponds to Δ_1/Δ_2 transition, and we can indeed label each carapace by its CBM character Δ_1, Δ_2, Δ_3. We term this transition occurring in the small strain region as the Δ switching. In this case, the linear deformation potential theory can be used to describe the strain effects on the band extremum (15). However, investigation of the large deformation points on its upper faces in Fig. 3*A* reveals that the CBM would not retain its location and major changes would happen.

Our ML model captures the occurrence of "L-Δ" transition across the $\beta_i - \alpha_j$ ridgelines where the CBM changes to "L" points in $\mathbf{k}$ space: $L_1 = (0.5, 0, 0)$, $L_2 = (0, 0.5, 0)$, $L_3 = (0, 0, 0.5)$; see Fig. 4 *A* and *B*, where for example, "Δ_3 carapace" changes to
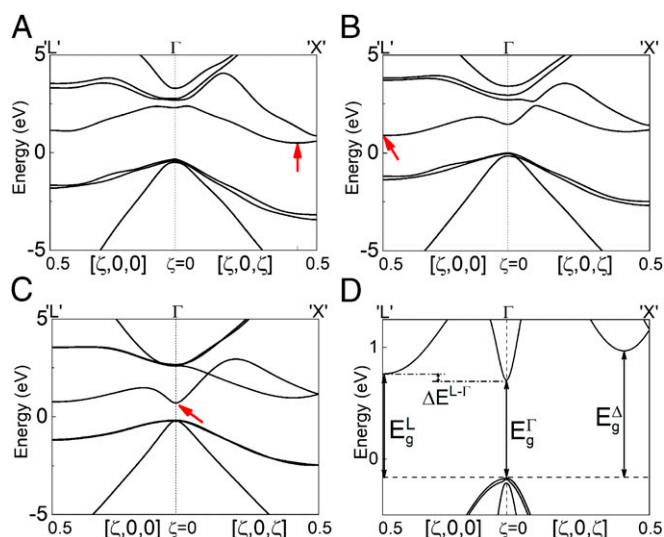
Fig. 4. Illustration of k-space transition in Si predicted by deep ESE. All of the transitions are verified by GW calculations. (*A* and *B*) Representation of the Δ-L transition. (*B* and *C*) The indirect-to-direct transition. The CBM (red arrows) locates at k point (0.433, 0.433, 0), (0.5, 0, 0), and (0, 0, 0) respectively. (*D*) The enlarged band structure around Fermi energy shows the competition of the three possible CBM positions. The three nonshear-strain cases for *A–C* are (−0.23, 1.84, 3.45%), (4.63, 8.23, 9.22%), and (9.85, 9.31, 9.4%), corresponding to points on the different faces of the bandgap isosurface in Fig. 3.

"L_1 carapace" across the $\alpha_1-\beta_3$ ridgeline, and "Δ_3 carapace" changes to "L_2 carapace" across the $\alpha_2-\beta_3$ ridgeline. None of the ridgelines or carapaces (e.g., Δ_3 carapace bound by $\mu-\alpha_1-\beta_3-\alpha_2-\mu$) are truly flat. The large, nonperturbative deformation makes the conventional theory ineffective in predicting it. Moving further toward χ in the strain space, CBM would remain at L and a cross-over of the $\chi_2 - \beta_j$ ridgelines is referred to as an L switching. Indirect-to-direct bandgap transition occurs near the upper tip of the paleolith-like isosurface where CBM appears at Γ, as shown in Fig. 4*C*. This can be explained by the competition between drops of different band edges. In general, as strain increases, the band edge at both Γ and L would decrease. As a result of high strains, the energy decrease at Γ is faster and eventually the bandgap becomes direct, as shown in Fig. 4*D*. In this case, we transition for example from the L_1 carapace ($\alpha_1-\beta_3-\chi_3-\chi_2-\beta_2-\alpha_1$ in Fig. 3*A*) to "Γ carapace" ($\chi_1-\chi_2-\chi_3-\chi_1$ in Fig. 3*A*) across the $\chi_2-\chi_3$ ridgeline. When the strained Si turns into a direct-bandgap semiconductor, it would exhibit a significant enhancement in its optical transitions around the fundamental adsorption edge compared with an undeformed Si, due to the elimination of phonon involvement to facilitate adsorption or emission. As absorbance increases exponentially with thickness in a material, a solar cell based on direct bandgap Si with high adsorption coefficient would require much less thickness to absorb the same amount of light, paving the way for the design of lightweight high-efficiency solar cells. *SI Appendix,* Table S2 summarizes all of the details of the $\mathbf{k}$-space transitions, thus resolving the conduction band properties exhaustively for a wide range of strains.

Incremental Fitting. We next show that our NN-based surrogate models can successfully learn from several datasets and assimilate them. This capability is becoming increasingly important with the spread of materials property databases that collect data from different studies (20). The incremental training of the NN starts from the same weights but is done on the extended dataset with the additional data included. We also increase the learning rate of stochastic gradient descent algorithm and regularizers (dropout rate and weight regularization) to circumvent limitations arising from the same local minima of the loss function established during the training on the initial dataset. This allows the model to

not only handle additional training on the incoming data appended to a database but to do it much faster than from scratch.

Numerical experiments conducted on the NN model demonstrate that incremental fitting of the models effectively reduces the error on a new dataset, see *SI Appendix*, Table S3. Such incrementally fitted models are, thus, equally applicable to the bandgap approximation and various optimization tasks. Moreover, these models may be reused when shifting to other materials such as Ge, since the implicit insights about symmetries, transitions, and extreme cases are stored in the parameters of NN. Training the model for the other material starting from the weights for Si would significantly reduce the time and amount of data needed due to knowledge transfer, also referred to as transfer learning (21), leading to rapid development of versatile surrogate models for ESE.

Discussion

ML models provide an efficient way of representing electronic band structure allowing for studies and accurate ESE predictions of a variety of physical phenomena such as band warping, degeneracy lifting, indirect-to-direct bandgap transition, and semiconductor-to-metal transition. In previous studies, bandgap engineering was conducted largely by tuning only one or two strain components. Our ML methods are capable of exploring the full spectrum of possibilities by efficiently analyzing highly nonlinear relations between electronic band dispersion and the strain tensor. To this end, the electronic band structure of silicon is accurately captured from ML through only a limited amount of calculations. Employing deep-NN algorithms, the bandgap of Si can be fitted as a function of strain within milli-electron-volt accuracy.

In prior approaches of analytically describing strain effects by traditional means, the linear deformation potential theory has often been invoked and its insufficiency at large deformation cases (Fig. 2A) makes it impossible to map out the entire strain space. By contrast, the general and systematic ML framework we demonstrate here makes the problem of representing the bandgap, and more broadly, the band structure, as a function of 6D strain computationally tractable. Many avenues remain for the application of our models on multiple fronts. Among these we mention the extension of the model to increasingly complex material structures, predicting their bandgap and band structure, and phonon and photonic band structure.

Different strains may result in the same bandgap, and in seeking a specific bandgap, or any other materials figure of merit, one should choose the strain with a minimal effort required given the

nonuniqueness of choice of a given target property or figure of merit. For this purpose, the DOB envelope we developed here is essential in understanding and fully utilizing deep ESE. In our work, we use the elastic strain energy density as a scalar metric or "norm" of the strain tensor for rationally choosing the ESE route that requires the least energy metastability and corresponds to the safest deformation manner in principle. For example, we have demonstrated that our model is able to locate the most energy-efficient pathway in the entire strain space to transform silicon from a semiconductor to a metal or to convert diamond from an ultrawide-bandgap material to a wide or even small-bandgap semiconductor. Latest advances in methods to apply large strains have included wide adoption of microelectromechanical systems and nanoelectromechanical systems, in situ indentation techniques, and nano-cantilever-beam bending (7, 8) and anviling (22) on materials across different size scales. The growing variety of technologies available to apply strains in a precisely controlled manner through mechanical, electrical, magnetic, thermal, and other means also promises the design of experiments to impose and tune different components of strains (23–26). Thanks to the expanding maturity of available tools, experimental implementation of the ESE approaches identified here for the 6D strain space is a next step in advancing further progress in this field. The distinctive ML model we propose here thus offers a potentially powerful method in guiding the design of approaches for a wide variety of semiconductor materials including silicon and diamond that could lead to performance improvement in applications as diverse as flexible electronics (27), nanomechanical resonators (28), optical fibers (23), and energy storage systems (29).

Methods

First-Principles Calculations. Details for DFT simulations are in *SI Appendix*, Note S2.

ML. NN and tree-based ensemble algorithms were adopted. More details are in *SI Appendix*, Note S2.

Data Fusion. Details for data fusion are in *SI Appendix*, Note S2.

1. Gilman JJ (2008) *Electronic Basis of the Strength of Materials* (Cambridge Univ Press, Cambridge, UK), 1st Ed.
2. Zhu T, Li J (2010) Ultra-strength materials. *Prog Mater Sci* 55:710–757.
3. Feynman RP (1960) There's plenty of room at the bottom. *Eng Sci* 23:22–36.
4. Li J, Shan Z, Ma E (2014) Elastic strain engineering for unprecedented materials properties. *MRS Bull* 39:108–114.
5. Qian X, Liu J, Fu L, Li J (2014) Solid state theory. Quantum spin Hall effect in two-dimensional transition metal dichalcogenides. *Science* 346:1344–1347.
6. Bedell SW, Khakifirooz A, Sadana DK (2014) Strain scaling for CMOS. *MRS Bull* 39:131–137.
7. Zhang H, et al. (2016) Approaching the ideal elastic strain limit in silicon nanowires. *Sci Adv* 2:e1501382.
8. Banerjee A, et al. (2018) Ultralarge elastic deformation of nanoscale diamond. *Science* 360:300–302.
9. Tsao JY, et al. (2018) Ultrawide-bandgap semiconductors: Research opportunities and challenges. *Adv Electron Mater* 4:1600501.
10. Perdew JP, Burke K, Ernzerhof M (1996) Generalized gradient approximation made simple. *Phys Rev Lett* 77:3865–3868.
11. Aryasetiawan F, Gunnarsson O (1998) The GW method. *Rep Prog Phys* 61:237–312.
12. Ramakrishnan R, Dral PO, Rupp M, von Lilienfeld OA (2015) Big data meets quantum chemistry approximations: The Δ-machine learning approach. *J Chem Theory Comput* 11:2087–2096.
13. Khaleghi B, Khamis A, Karray FO, Razavi SN (2013) Multisensor data fusion: A review of the state-of-the-art. *Inf Fusion* 14:28–44.
14. Baliga BJ (1982) Semiconductors for high-voltage, vertical channel field-effect transistors. *J Appl Phys* 53:1759–1764.
15. Bardeen J, Shockley W (1950) Deformation potentials and mobilities in non-polar crystals. *Phys Rev* 80:72–80.
16. Capasso F (1986) Compositionally graded semiconductors and their device applications. *Annu Rev Mater Sci* 16:263–291.

17. Chang KYS, von Lilienfeld OA (2018) AlxGa1-xAs crystals with direct 2 eV band gaps from computational alchemy. *Phys Rev Mater* 2:073802.
18. Shockley W, Queisser HJ (1961) Detailed balance limit of efficiency of p-n junction solar cells. *J Appl Phys* 32:510–519.
19. Jenkins DP (1956) Calculations on the band structure of silicon. *Proc Phys Soc A* 69:548–555.
20. Jain A, et al. (2013) Commentary: The materials project: A materials genome approach to accelerating materials innovation. *APL Mater* 1:011002.
21. Pan SJ, Yang Q (2010) A survey on transfer learning. *IEEE Trans Knowl Data Eng* 22:1345–1359.
22. Li B, et al. (2018) Diamond anvil cell behavior up to 4 Mbar. *Proc Natl Acad Sci USA* 115:1713–1717.
23. Healy N, et al. (2014) Extreme electronic bandgap modification in laser-crystallized silicon optical fibres. *Nat Mater* 13:1122–1127.
24. Feng J, Qian X, Huang C-W, Li J (2012) Strain-engineered artificial atom as a broad-spectrum solar energy funnel. *Nat Photonics* 6:866–872.
25. Aage N, Andreassen E, Lazarov BS, Sigmund O (2017) Giga-voxel computational morphogenesis for structural design. *Nature* 550:84–86.
26. Lian H, Christiansen AN, Tortorelli DA, Sigmund O, Aage N (2017) Combined shape and topology optimization for minimization of maximal von Mises stress. *Struct Multidiscipl Optim* 55:1541–1557.
27. Grumstrup EM, et al. (2014) Reversible strain-induced electron-hole recombination in silicon nanowires observed with femtosecond pump-probe microscopy. *Nano Lett* 14:6287–6292.
28. Ovartchaiyapong P, Lee KW, Myers BA, Jayich ACB (2014) Dynamic strain-mediated coupling of a single diamond spin to a mechanical resonator. *Nat Commun* 5:4429.
29. Yu D, Feng J, Hone J (2014) Elastically strained nanowires and atomic sheets. *MRS Bull* 39:157–162.

SI Appendix

Deep Elastic Strain Engineering of Bandgap through Machine Learning

Zhe Shi [1,*], Evgenii Tsymbalov [2,*], Ming Dao [1], Subra Suresh [3], Alexander Shapeev [2], Ju Li [1]

[1]Department of Materials Science and Engineering and Department of Nuclear Science Engineering, Massachusetts Institute of Technology, Cambridge, Massachusetts 02139, USA
[2] Skolkovo Institute of Science and Technology, Moscow 121205, Russia
[3]Nanyang Technological University, Singapore 639798, Republic of Singapore
*These authors contributed equally.
[⊥] SSuresh@ntu.edu.sg, A.Shapeev@skoltech.ru, liju@mit.edu

SI Appendix, Note S1: Straining of diamond cubic crystals in real and reciprocal space

The straining can be best described by applying a 3×3 tensor transformation to the perfect silicon or diamond primitive cell to avoid the confounding effect of band folding in larger supercells which causes difficulty in identifying band structure information (1). Due to material anisotropy, we present all the related figure of merit results within 6D strain space instead of 3D space of principal strains. To avoid redundant computations, we ensured that each strain we applied to a crystal has a one-to-one correspondence to a distinct deformation case. The non-translational part of a homogeneous deformation of a crystal can be defined by a second-order deformation gradient tensor $\mathbf{F}$, which can be viewed as the Jacobi matrix linking deformed and underformed lattice vectors. The relationship between the symmetric strain tensor $\boldsymbol{\varepsilon}$ and $\mathbf{F}$ is given by $\boldsymbol{\varepsilon} = \frac{1}{2}(\mathbf{F} + \mathbf{F^T}) - \mathbf{I}$. Since the band structure does not change upon rotations of the crystal, we can eliminate the rotational degrees of freedom by adopting upper triangular $\mathbf{F}$ to map out all deformation cases, as in SI Appendix, Figure S1a.

Under general 3D three-normal-strains deformation, the original O_h crystal point group of Si turns into a D_{2h} point group. The Brillouin zone for deformed Si in this case is shown in SI Appendix, Figure S1b. In general it is not anymore a regular truncated octahedron with equilateral hexagonal and square faces. The reciprocal space lattice vectors are adjusted by the inverse transpose of the deformation gradient tensor in real space, i.e. $\mathbf{F}^{-T}$, as a result of the deformation. The center of any type of Brillouin zone is labeled as Γ and we keep this tradition. In undeformed Si, the centers of the square and regular hexagonal surfaces on the Brillouin zone boundary are completely degenerate and labeled as X and L, respectively. For the simplicity of comparison, we follow the same spirit and still denote the 'X'-type points as the centers of the tetragon surfaces and L-type points as the centers of the regular/non-regular hexagonal surfaces. The lines that connect the Γ point to the 'X'-type points are labeled as 'Δ'-type. This way, the six 'X'- and 'L'-type points, though non-degenerate, would keep the correct fractional coordinates of $\langle 0.5,0,0.5 \rangle$- and $\langle 0.5,0,0 \rangle$-type, and the **k**-points along the Γ-'X' line would all have the $\langle \zeta, 0, \zeta \rangle$-type coordinates. As the CBMs of our concern always appear on either the center of the Brillouin zone, center of the zone boundary surfaces, or the line connecting the zone center and surface center, our notations are sufficient.

SI Appendix, Note S2:

First-principles calculations
We used the Perdew-Burke-Ernzerhof (PBE) (2) exchange-correlation functional and the projector augmented wave method (PAW) (3) in our DFT simulations implemented in the Vienna Ab initio Simulation Package (4) with spin-orbit coupling incorporated. A plane wave basis set with an energy cutoff of 520 eV was adopted to expand the electronic wavefunctions. The Brillouin zone integration was conducted on a $13 \times 13 \times 13$ Monkhorst-Pack $\boldsymbol{k}$-point mesh ($6 \times 6 \times 6$ for GW calculations). Atomic coordinates in all the structures were relaxed until the maximum residual force was below 0.0005 eV Å^{-1}. We focused on the strain range of $\{-5\% \leq \varepsilon_j \leq 10\%,\ j = 1 \dots 6\}$ for silicon and $\{-5\% \leq \varepsilon_j \leq 5\%,\ j = 1 \dots 6\}$ for diamond. The large strain values and corresponding strain energy density values are on the same order of magnitude compared to those achieved experimentally for bulk silicon and bulk diamond and these strains are all below theoretical failure strains, i.e. without phonon instability occurring.

Machine learning
Neural network (NN)
NN fitting is implemented within the Tensorflow (5) framework. To predict the bandgap we used deep NNs with four hidden layers with a (64 - 128 - 256 - 256) structure in the case of three-normal-strains strains ($\boldsymbol{\varepsilon^{3D}}$) and a (512 - 256 - 256 - 256) structure for the case with shear strains ($\boldsymbol{\varepsilon^{6D}}$), as shown in main text Figure 1a and SI Appendix, Figure S2. For the more complicated task of band energy prediction at a single $\boldsymbol{k}$-point, the architecture of (512 - 256 - 256 - 256) was used. The leaky rectified linear unit was chosen as an activation function. We used the Adam stochastic optimization method, the orthogonal weight initialization (6) and the dropout technique to prevent overfitting.
Tree-based ensemble algorithms
The algorithms were implemented in Scikit-learn (7). For our regression task, we used two types of ensembling on decision trees: the random forest regression (8) and the gradient boosting regression (9). The architecture is shown in SI Appendix, Figure S2. Hyper-parameters tuning was executed by using cross-validation on a training set to enhance the fitting process.

Data fusion
Data fusion represents the concept of combining different data sources in order to improve the model (10). We adopted this approach to further improve the learning outcome of E_g, namely the most technically important property for an electronic material. While the data fusion model prediction in Ref. (11) corresponds to a baseline value plus a correction, our data fusion approach is more advanced. More specifically, given E_g^{PBE} computed using an approximate baseline level of theory (PBE) at a particular query strain case, a related E_g^{GW} value corresponding to a more accurate and more demanding target level of theory (GW) can be estimated as a function of both E_g^{PBE} and $\boldsymbol{\varepsilon}$. Therefore, the E_g^{GW} consistent with the query

strain case is learned using exclusively $\boldsymbol{\varepsilon}$ and E_g^{PBE} as input, as illustrated in Figure 1a and b. The resulting data fusion model reduces the MAE in the prediction of bandgap by more than half for kernel-based ensemble methods and allow the bandgap predicted by NN be reach an extremely high accuracy of 8 meV, as shown in main text Figure 1b and SI Appendix, Table S1.

SI Appendix, Note S3:

Ranking of common Si crystal direction families for obtaining the same target bandgap through uniaxial compressive straining (from the most energy efficient strain direction to the least energy efficient strain direction):

 <111>, <332>, <322>, <221>, <211>, <321>, <331>, <320>, <210>, <311>, **<110>**, <310>, **<100>**

Ranking of common Si crystal direction families for obtaining the same target bandgap through uniaxial tensile straining (from the most energy efficient strain direction to the least energy efficient strain direction):

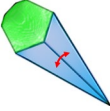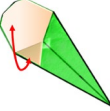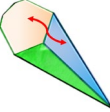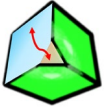 **<111>**, <332>, <221>, <322>, <331>, <211>, <311>, <321>, **<110>**, <320>, <210>, <310>, **<100>**

SI Appendix, Table S1:

Table S1: MAE and RMSE (in units of eV) for ML algorithms for bandgap prediction with or without the Δ-ML model. Here, the Lagrange polynomial of degree 8 is used. Relative error: norm of the difference between the true value and the prediction divided by the norm of the true value.

ML algorithms	GW		GW+PBE (Δ-ML)	
	MAE	RMSE	MAE	RMSE
Lagrange	0.0211	0.0274	0.0186	0.0241
GBR	0.0334	0.0521	0.0135	0.0209
RFR	0.0434	0.0596	0.0145	0.0215
NN	0.0099	0.0144	0.0080	0.0118
NN relative error	1.72%	2.78%	1.38%	2.05%

SI Appendix, Table S2:

Table S2: **k**-space CBM transitions. Each of 12 separating ridgelines of the iso-bandgap body tabulated. The constants k_1 and k_2 are approximately equal to 0.425 and 0.5, corresponding to points on Δ and L, respectively.
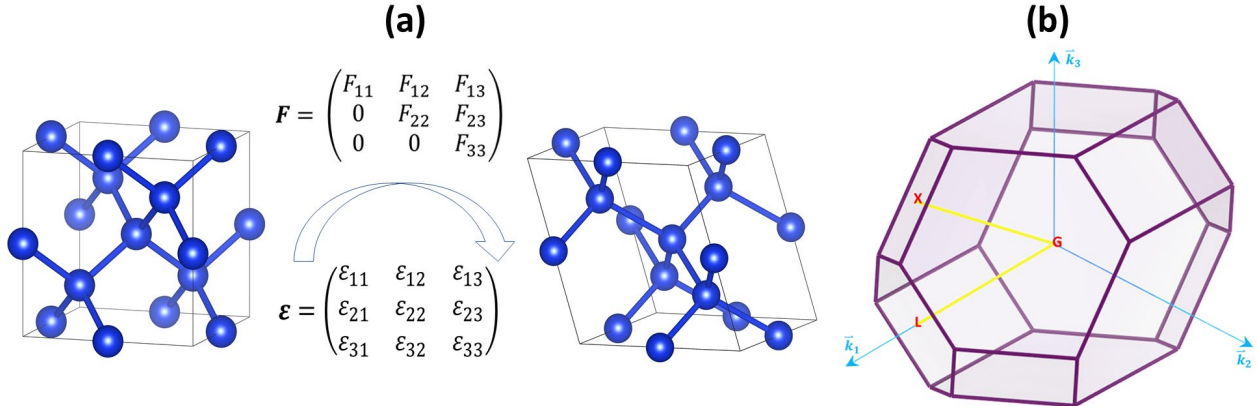
Type	Change of "carapace"		**k**-coordinate of CBM
'Δ'-switching		$\Delta_1 \leftrightarrow \Delta_2$	$(0, k_1, k_1) \leftrightarrow (k_1, 0, k_1)$
		$\Delta_2 \leftrightarrow \Delta_3$	$(k_1, 0, k_1) \leftrightarrow (k_1, k_1, 0)$
		$\Delta_3 \leftrightarrow \Delta_1$	$(k_1, k_1, 0) \leftrightarrow (0, k_1, k_1)$
'L'-switching		$L_1 \leftrightarrow L_2$	$(k_2, 0, 0) \leftrightarrow (0, k_2, 0)$
		$L_2 \leftrightarrow L_3$	$(0, k_2, 0) \leftrightarrow (0, 0, k_2)$
		$L_3 \leftrightarrow L_1$	$(0, 0, k_2) \leftrightarrow (k_2, 0, 0)$
'L-to-Δ' transition		$L_1 \leftrightarrow \Delta_2$	$(k_2, 0, 0) \leftrightarrow (k_1, 0, k_1)$
		$L_1 \leftrightarrow \Delta_3$	$(k_2, 0, 0) \leftrightarrow (k_1, k_1, 0)$
		$L_2 \leftrightarrow \Delta_1$	$(0, k_2, 0) \leftrightarrow (0, k_1, k_1)$
		$L_2 \leftrightarrow \Delta_3$	$(0, k_2, 0) \leftrightarrow (k_1, k_1, 0)$
		$L_3 \leftrightarrow \Delta_1$	$(0, 0, k_2) \leftrightarrow (0, k_1, k_1)$
		$L_3 \leftrightarrow \Delta_2$	$(0, 0, k_2) \leftrightarrow (k_1, 0, k_1)$
Indirect-to-direct bandgap transition		$L_1 \leftrightarrow \Gamma$	$(k_2, 0, 0) \leftrightarrow (0, 0, 0)$
		$L_2 \leftrightarrow \Gamma$	$(0, k_2, 0) \leftrightarrow (0, 0, 0)$
		$L_3 \leftrightarrow \Gamma$	$(0, 0, k_2) \leftrightarrow (0, 0, 0)$

SI Appendix, Table S3:

Table S3: Si bandgap prediction errors, RMSE and MAE (in units of eV), for the incremental fitting scenario on reduced datasets. The error in both metrics is reduced for both ε^{3D} and ε^{6D} datasets after the incremental fitting.

	ε^{3D}		ε^{6D}	
	before	after	before	after
RMSE	0.0403	0.0069	0.0264	0.0253
MAE	0.0167	0.0052	0.0179	0.0167

SI Appendix, Figure S1:

Figure S1: (a) ESE achieved by applying a reduced deformation gradient tensor to the undeformed diamond cubic lattice of Si or C in the real space. (b) Brillouin zone of diamond cubic crystal under three-normal-strains deformation. It is a tetradecahedron with 8 hexagonal and 6 quadrilateral faces. The discussions based on Figure 5 of the main text incorporate the same labels and **k** coordinates as here.
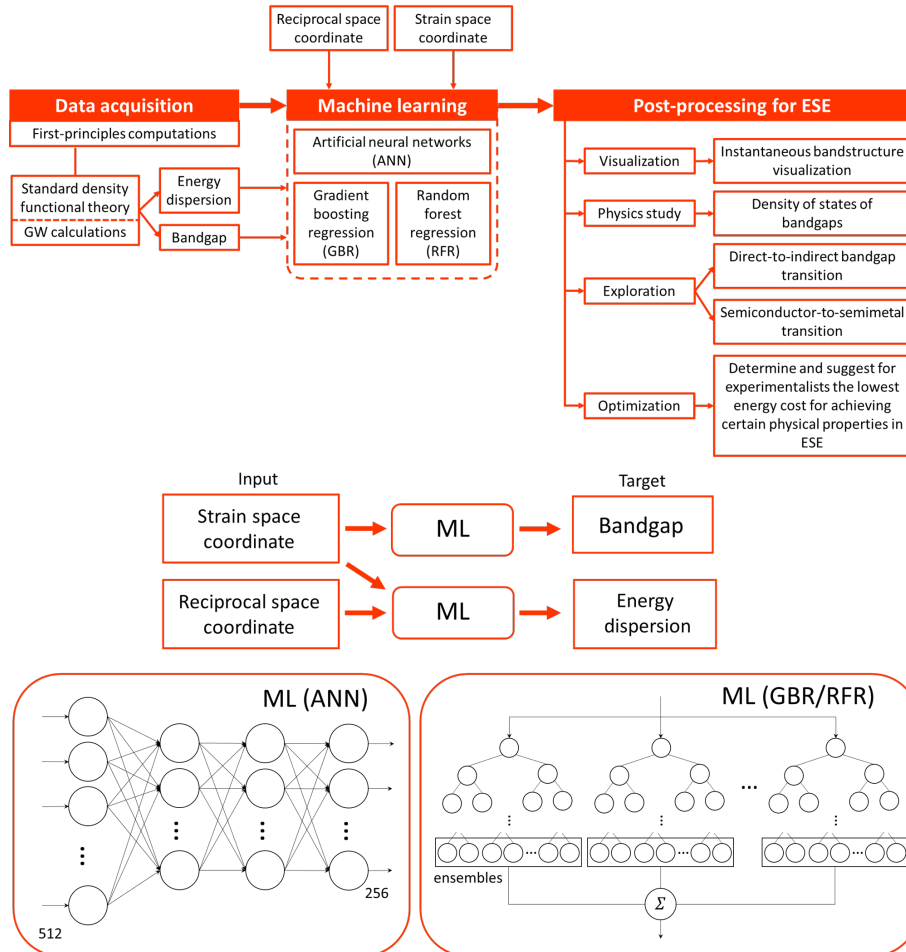
SI Appendix, Figure S2:

Figure S2: *Top:* Three major processing steps involved in the deep ESE of bandgap, including data acquisition through *ab initio* computations, ML and physical property exploration. *Middle*: Flowchart setting out the details of the ML process. Here, strain tensor and **k** coordinate are used as the input whereas the bandgap and energy dispersion are the target for fitting. For the ML algorithms, our set-up supports ANN, GBR, RFR, and other kernel-based fitting methods. *Bottom*: Detailed architecture of the algorithms adopted.
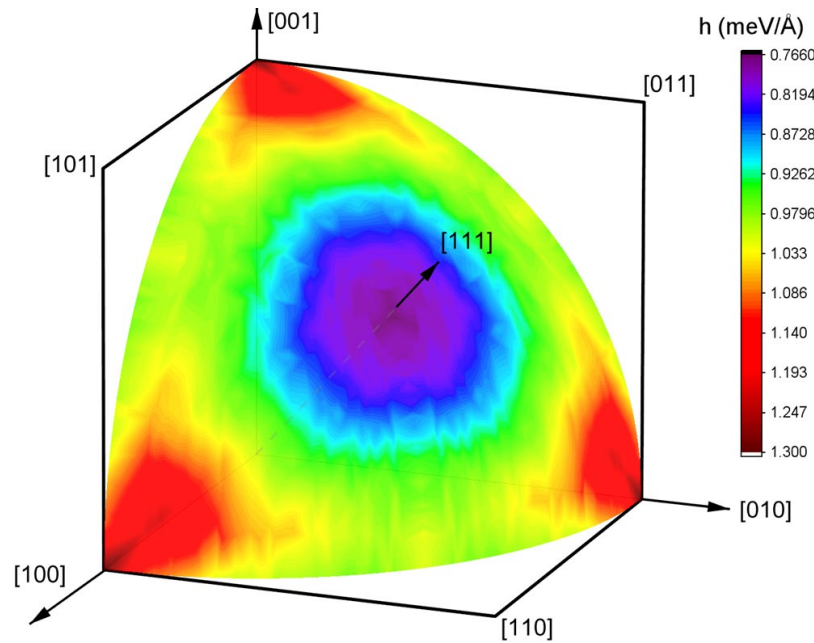
SI Appendix, Figure S3:

Figure S3: Color contour map of the elastic strain energy density (h) required to reach the same bandgap level of 0.6 eV through uniaxial compressive straining in Si.

References:

1. Umeno Y, Kushima A, Kitamura T, Gumbsch P, Li J (2005) Ab initio study of the surface properties and ideal strength of (100) silicon thin films. *Phys Rev B* 72(16):165431.

2. Perdew JP, Burke K, Ernzerhof M (1996) Generalized Gradient Approximation Made Simple. *Phys Rev Lett* 77(18):3865–3868.

3. Blöchl PE (1994) Projector augmented-wave method. *Phys Rev B* 50(24):17953–17979.

4. Kresse G, Furthmüller J (1996) Efficiency of ab-initio total energy calculations for metals and semiconductors using a plane-wave basis set. *Comput Mater Sci* 6(1):15–50.

5. Abadi M, et al. (2016) TensorFlow: A System for Large-scale Machine Learning.

Proceedings of the 12th USENIX Conference on Operating Systems Design and Implementation, OSDI'16. (USENIX Association, Berkeley, CA, USA), pp 265–283.

6. Saxe AM, McClelland JL, Ganguli S (2013) Exact solutions to the nonlinear dynamics of learning in deep linear neural networks. *ArXiv13126120 Cond-Mat Q-Bio Stat*. Available at: http://arxiv.org/abs/1312.6120 [Accessed October 8, 2018].

7. Pedregosa F, et al. (2011) Scikit-learn: Machine Learning in Python. *J Mach Learn Res* 12:2825–2830.

8. Breiman L (2001) Random Forests. *Mach Learn* 45(1):5–32.

9. Friedman JH (2001) Greedy Function Approximation: A Gradient Boosting Machine. *Ann Stat* 29(5):1189–1232.

10. Khaleghi B, Khamis A, Karray FO, Razavi SN (2013) Multisensor data fusion: A review of the state-of-the-art. *Inf Fusion* 14(1):28–44.

11. Ramakrishnan R, Dral PO, Rupp M, von Lilienfeld OA (2015) Big Data Meets Quantum Chemistry Approximations: The Δ-Machine Learning Approach. *J Chem Theory Comput* 11(5):2087–2096.